RSC Advances

ROYAL SOCIETY OF CHEMISTRY

www.rsc.org/advances

Comparative supercapacitance performance of CuO nanostructures for energy storage device applications

V. Senthilkumar,[1] Yong Soo Kim,[1*] S.Chandrasekaran,[2] Balasubramaniyan Rajagopalan,[2] Eui Jung Kim,[2] and Jin Suk Chung[2]

[1] Department of Physics and Energy Harvest Storage Research Center (EHSRC), University of Ulsan, Ulsan 680-749, South Korea.

[2]School of Chemical Engineering, University of Ulsan, Ulsan 680-749, South Korea.

*Corresponding Authors: yskim2@ulsan.ac.kr (Y.S. Kim)

Abstract

In the present study, three different morphologies of copper oxide (CuO) nanostructures; bud-, flower- and plate-shaped CuOs were synthesized by simple chemical method. Binder-included pseudocapacitor electrodes were prepared using bud- and flower-shaped CuOs whereas, directly grown CuO-nanoplates on Ni foam was used as binder-free electrode in a three-electrode setup for electrochemical studies. Remarkably, the binder-free CuO nanoplates electrode exhibited excellent specific capacitance of 536 Fg^{-1} at the current density of 2 Ag^{-1} whereas, binder-included electrodes of bud- and flower-shaped CuO exhibited 230 Fg^{-1} and 296 Fg^{-1} respectively, at a current density of 0.7 Ag^{-1} in a 6M KOH electrolyte. The cycling retention test and charge/discharge stability for binder-free CuO nanoplates electrode showed 94% capacity retention after 2000 cycles and the capacitance loss of only 11.3% over ~1000 cycles at current density of 4 Ag^{-1} from charge/discharge measurements. Also, binder-free CuO electrode showed a higher energy and power density of 29.4 Wh/kg and 12.7 W/kg respectively, at 1.96 Ag^{-1} in an asymmetrical device, when compared to the binder-included electrode of flower-shaped CuO.

1. Introduction

With an increasing demand of fossil fuels and global warming issues, clean energy era has plunged into this present scenario that includes the electrochemical energy storage devices comprising of the fuel cells, batteries and supercapacitors[1-2]. The long used batteries over decades have a low power density (i.e. slow charge-discharge rates) and a high energy density; while in contrast, the conventional dielectric capacitors possess a high power density but lack a large energy density. Hence, it is now a mandatory necessity to develop systems which can simultaneously provide high energy density as well as high power density[3].

In recent years, the electrochemical supercapacitors have gained significant research interest for its high power density, reversibility and long cycle life[4-5]. The supercapacitors are broadly classified based on their storage mechanism, the electrical double layer capacitor (ELDC) and pseudocapacitor. The non-Faradaic reaction with accumulation of charges through electrostatic interaction at the electrode/electrode interface forms the base of the energy storage mechanism of the EDLC, and that of the pseudocapacitor is due to the fast Faradaic redox reaction on the surface of electro-active materials[6-7]. Till date, the widely used electrode in EDLCs are the carbon based materials, due to their good processing ability, large surface area/porosity, good cycle life, and low cost[8-9], but the devices so fabricated suffer from their relatively lower capacity in storing charge.

In contrast, the electrochemical pseudocapacitors have shown to possess higher electric conductivity and faster cation dispersion, thus resulting in a much higher power densities and energy densities[10-14]. Transition metal oxides presenting a rich redox reaction are the class of ideal supercapacitor electrode materials that have drawn intense interest recently among other materials[15-16]. Previously, hydrous ruthenium oxides (RuO) were used as electrode materials.

However, the high cost of the materials limits their application in large scale manufacturing sector. Hence, efforts have been focused in the search of an alternative and cheaper electrode materials including, NiO[17], Co_3O_4 [18] and MnO_2[19] to explore their ability in the construction of supercapacitors with enhanced energy and power densities. Among these metal oxides, CuO is a promising candidate due to their cost effectiveness, abundant resources, eco-friendly nature, and simple methods for the preparation of various nanosized dimensions. Its application as electrode material for rechargeable Li-ion batteries[20] showed remarkably high Li-ion storage capacities, through a redox reaction. Recently few works have been investigated for the CuO as pseudocapacitor electrode applications [21-23]. However, compared to the other metal oxides, the reported capacitance values for CuO electrodes are still low (<32%) though it has a high theoretical capacitance values around 1783 F/g within the window of 0.68 V[24].

Herein, we report a facile, cost-effective and scalable synthesis approach to prepare three different morphologies of CuO nanostructures; bud-, flower- and plate-shaped CuOs by simple chemical method. The morphological, structural and electrochemical properties of the obtained CuO nanostructures were investigated. The bud- and flower-shaped CuOs were prepared in powder form by a simple hydrothermal method and those powders were used for the electrode preparation with the help of binder (PVDF), whereas binder-free seed mediated grown CuO nanoplates on Ni foam was directly used as electrode for electrochemical studies. Remarkably, the seed mediated grown binder-free CuO nanoplates electrode exhibited promising specific capacitance and excellent capacitance retention during cycling test.

2. Experimental

2.1 Synthesis of bud and flower -shaped CuO nanostructures

Copper oxide nanostructures were synthesized as suggested by Pike et al.[25] with slight modifications. In brief, the aqueous solutions of copper nitrate ($Cu(NO_3)_2 \cdot 3H_2O$) and hexamethylenetetramine (HMT) ($C_6H_{12}N_4$) were mixed separately with deionized water to an equal molar concentration of 0.02 M. The solutions were stirred separately for 30 min and then mixed uniformly. The mixture was kept at 120°C for 6 and 18 hours of reaction time. The precipitated product thus formed was collected and washed with methanol several times to remove the ionic impurities. Finally, the collected powders were annealed at 400°C for an hour and the obtained powder was used for the further analysis and capacitance studies.

2.2 Seed mediated growth of copper oxide nanoplates on Ni foam

Synthesis of CuO nanoplates on Ni foam (Density-320 g/m^2, Pore size-680 µm, Thickness-1.7 mm, Hittite co., ltd, S.Korea) was carried out by using a CuO nanoseed-mediated growth method. In a typical process, CuO nanoseed particles were first grown on Ni foam via an alcohothermal method. After standard cleaning process, Ni foam was immersed in a 25 mM ethanolic solution of copper(II)acetate($Cu(CO_2CH_3)_2$) at 60°C for 45mins. The Ni foam was then air-dried and annealed at 250°C for 30mins to obtain a CuO nanoseed layer. Next, to form the CuO nanoplates, the above substrate was vertically dipped in an equimolar solution (13mM) of copper nitrate trihydrate and HMT in deionized (DI) water at 120°C for 16 hours. The substrate was then taken out from the growth solution and a homogeneous red brown layer was observed over the surface of Ni foam. Finally, the samples were rinsed with DI water gently several times and annealed at 400°C for an hour in air. The weight of the deposited CuO was accurately calculated from the difference in the weight of the substrate before the chemical bath process and with CuO loading after calcinations using an analytical micro balance. The weight was found to be 2.4 mg/cm^2.

The prepared final CuO products were analyzed with various characterization tools. The structural and morphological studies were done by X-ray diffraction (Rigaku-X-ray diffractometer with Cu Kα radiation), and field emission-scanning electron microscopy (JEOL JSM 6500F) analysis. The optical and chemical composition was investigated using Raman (Thermo Scientific DXR Raman spectrophotometer) and X-ray photoelectron spectroscopy (XPS, Theta Probe AR-XPS System, Thermo Fisher Scientific) analysis. The surface area and porosity of the sample was confirmed using Brunauer-Emmett-Teller (BET-micromeritics ASAP 2020) measurements.

2.2 Electrochemical measurements

The electrochemical measurements were performed using a computerized potentiostat (IvimStat, IVIUM Tech.) under ambient conditions. A typical electrochemical measurement with a three-electrode cell system was employed, that composed of CuO as the working electrode, a platinum plate as the counter electrode, and an Ag/AgCl as the reference electrode**.** In the case of CuO powder, the working electrode was fabricated by mixing 80 wt% as-prepared CuO with 10 wt% carbon black and 10 wt% polyvinylidene fluoride (PVDF), and slurry of the above mixture was painted onto a clean Cu foil (1cm × 1cm) to act as the current collector. The loading mass of each of the binder included CuO electrodes were around 0.6 mg/cm^2. The coated film was then dried in a vacuum cabinet at 80°C, kept overnight to remove the excess solvent and water. Whereas, CuO film on Ni foam (1cm × 1cm) was directly used as the working electrode.

3. Results and discussion

3.1 Characterizations and growth process of CuO nanostructures

FE-SEM images and their corresponding energy-dispersive X-ray (EDX) spectra of the hydrothermally grown CuO nanostructures in two time interval are shown in Fig. 1(a-c) and (e-g), respectively. The images depict that the reaction time clearly influences the morphological changes of CuO. The bud-shaped CuO (Cu/CuO-1) nanostructures were obtained when the hydrothermal reaction proceeded for 6 hrs and the typical SEM images in different magnifications are as shown in Fig. 1(a-c). On extending the reaction time to 18 hrs, flower-shaped CuO (Cu/CuO-2) was obtained as shown in Fig. 1(e-g). The size of the flowers was approximately in the range of 10~15 μm. The view of the single flower-shaped structure is shown in Fig. 1(g), it clearly reveals the flowers to consist of many triangular-shaped petals. The diameter of the petals from the base to the tip showed variations, i.e. sharpened tips with wider bases. The wider base of the petals connected to each other, rooted in one center to finally form a beautiful flower-like morphology. Fig. 1 (i-k) shows the SEM images of the CuO nanoplates (Ni/CuO) grown uniformly on the nickel foam and the SEM image at lower magnification shows the CuO to form a uniform film all over the substrate. The SEM image at higher magnification indicates the majority of the nanoplates to be orientated almost vertically to the nickel foam substrate. The thickness of a single nanoplate was up to around 20 nm. EDX spectra (Fig. 1(d), (h) and (l)) clearly demonstrated the presence of Cu and O peaks and quantitative analysis revealed that the Cu and O were almost in a stoichiometry for all the CuO nanostructures.

XRD analysis was used for investigating the structure of the synthesized samples. Fig.2 (a) depicts typical XRD patterns of the samples synthesized in hydrothermal method and CuO-nameplates directly grown on Ni foam. In the XRD pattern, when compared with the standard diffraction peaks from JCPDS card no. 5-0661, the peaks located at 2θ values of 20–80° were indexed to the characteristic diffractions of monoclinic phase CuO. The peak intensities and width clearly indicated the sample to be highly crystalline in nature. The absence of other characteristic peaks, which could belong to the impurities such as $Cu(OH)_2$ or Cu_2O, indicated that the obtained product was phase-pure. Therefore, it was obvious that the sample composed of a pure monoclinic phase CuO, which is consistent with the EDX analysis.

Raman spectroscopy, which is a sensitive probe to the local atomic arrangements and vibrations of the materials, has been widely used to investigate the microstructural nature of the nanosized materials[26]. Figure 2(b) shows the Raman spectra of Cu/CuO-1 and Cu/CuO-2 morphologies. It showed the presence of three Raman peaks at 289.3, 338.5 and 622.7 cm^{-1}, with the second one being the weakest and the third being broad. In comparison with the vibrational spectra of a CuO single crystal[27], the peak at 289.3 cm^{-1} can be assigned to the A_g mode whereas, the peaks at 338.5 and 622.7 cm^{-1} to the B_g modes, which are comparable to the reported data for nanocrystal CuO[28]. In addition, a broadened peak at 1120 cm^{-1} was observed, which can be assigned to the multi-phonon (MP) transition of CuO nanostructure[27]. Therefore, from the Raman analysis it was evident that the synthesized product consists of single-phase CuO with a monoclinic structure.

To further confirm the elemental composition of prepared CuO nanostructures, XPS analysis was used to determine oxidation state of the Cu. All the binding energies obtained in the XPS analysis was calibrated using the C 1*s* signal at 284.5 eV used as a reference to correct any electrical charging effect of the sample surface. Fig. 2(c) shows the Cu 2*p* and O 1*s* core–level spectra of the Cu/CuO-2 sample. The Cu 2*p* core-level spectrum represents two peaks located at 934.3 and 954.3 eV which corresponds to the Cu $2p^{3/2}$ and Cu $2p^{1/2}$, respectively. These values corresponds with the data reported for the Cu 2*p* in CuO[29-31]. Also, the width of approximately 20 eV between these two Cu peaks is the same as in the standard spectrum of Cu. In addition to the Cu $2p^{3/2}$ and $2p^{1/2}$peaks, typical CuO-satellite peaks appear at binding energies with intense shake-up satellite peaks at 941.7 and 944.2 eV, these two peaks overlapping, and the existence of a strong satellite pattern at 962.6 for the Cu 2*p* rules out the possibility of the presence of Cu_2O phase[32-33]. Since the 3*d* shell is expected to be completely filled in Cu_2O, the shakeup satellite peaks indicate the presence of an unfilled Cu $3d^9$ shell, i.e., the existence of CuO at the surface[29-30,34]. From the O 1*s* core level spectrum, the low binding energy peak at 529.5 eV is due to the oxygen in the CuO crystal lattice, which corresponds to the O-Cu bond, whereas the higher binding energy peak at 531.5 eV is due to the different chemical states of oxygen, such as surface hydroxide due to adsorbed water from the atmosphere[35]. Thus, the XRD, Raman and XPS results support the fact that the nanostructures are composed mainly of CuO.

The specific surface areas and the porous nature of the powder samples are determined by measuring nitrogen adsorption–desorption isotherms as presented in Fig. 1(d) with the inset showing their corresponding pore size distribution (BJH). By comparing the isotherms and pore size distributions, it can be seen that the isotherm of the Cu/CuO-2 shows a wide hysteresis loop at a relative pressure range of 0.7–1.0 P/P_0 and the corresponding BET specific surface area is calculated to be ~30.6 m^2g^{-1} which is larger than that of the specific surface area (about 24.9 m^2g^{-1}) of the Cu/CuO-1 structure. In addition, the mesopore size distributions based on the BJH method of both samples are further confirmed by the corresponding pore size distribution curves (inset in Fig. 1(d)). The high surface area and mesoporous structure of the Cu/CuO-2 when compared to Cu/CuO-1, which provides the opportunity for the efficient diffusion and transportation of the electrolyte with the help of large pore channels, while the small pores provided more active sites for chemical reactions[36].

3.2 Electrochemical analysis of CuO nanostructures

The electrochemical analysis for all the CuO electrodes were conducted in aqueous 6M KOH solution. The merit of the use of alkali KOH electrolytes when compared to other organic electrolytes is due to their higher ionic concentration and lower resistance[12]. Fig. 3(a) shows the CV curves of the bare Cu and nickel foam substrates at a voltage scan rate of 5 mVs$^{-1.}$ Both the substrates exhibited small area of CV curve, and anodic and cathodic peak currents, lesser than 300 μA. These results clearly suggested that the capacitance contribution from both the substrates was minimal. Fig. 3(b-d) shows the capacitance performance of the Cu/CuO-1, Cu/CuO-2 and Ni/CuO electrodes evaluated with cyclic voltammograms at different scan rates of 5, 10, 20, 30, 50 and 100 mVs^{-1} at room temperature. The current under curve slowly increased with scan rate in all the electrodes. This behavior clearly shows the voltammetric current to be directly proportional to the scan rates of CV indicating an ideal capacitive behavior[37]. When there is an increase of the scan rate, the anodic peaks shift towards the positive potential whereas the cathodic peaks shift towards the negative potential. This phenomenon demonstrates the quasi-reversible nature of the redox reaction. The plot of cathodic peak current (i_p) against $v^{1/2}$ (inset Fig. 3(b-d)) shows a nearly linear correlation, which suggests a diffusion-controlled electrode reaction with the electrolyte used[22].

The pseudocapacitance of transition metal oxides has been attributed to redox transitions of species at various oxidation states[38]. Therefore, based on the present CV data and previously reported experimental results, the charging and discharging processes in the CuO electrode in alkaline (KOH) electrolyte at the potential range of 0–0.6 V can be summarized in the following reactions[24, 39-40].

$$\frac{1}{2}\mathrm{Cu_2O} + \mathrm{OH^-} \Leftrightarrow \mathrm{CuO} + \frac{1}{2}\mathrm{H_2O} + e^- \qquad (1)$$

$$\frac{1}{2}\mathrm{Cu_2O} + \frac{1}{2}\mathrm{H_2O} + \mathrm{OH^-} \Leftrightarrow \mathrm{Cu(OH)_2} + e^- \qquad (2)$$

$$\mathrm{CuOH} + \mathrm{OH^-} \Leftrightarrow \mathrm{CuO} + \mathrm{H_2O} + e^- \qquad (3)$$

$$\mathrm{CuOH} + \mathrm{OH^-} \Leftrightarrow \mathrm{Cu(OH)_2} + e^- \qquad (4)$$

The capacitive performances of all the electrodes were evaluated with constant current charge/discharge measurements at different current densities as shown in Fig. 4(a-c). In order to avoid the occurrence of oxygen evolution, the electrode was charged and discharged within the potential range of 0-0.5 V vs Ag/AgCl. The charge/discharge curves showed a good symmetry with nearly triangular shaped curves for all current densities, which elucidated the good capacitive characteristics of the material even at high current density. The specific capacitance (C_s) of an electrode in a given electrolyte solution can be calculated using the following equation[21-22].

$$C_s = \frac{I \times \Delta t}{m \times \Delta V} \qquad (5)$$

where, I (mA) is the discharge current for the applied time duration Δt (s), ΔV (V) is the potential window, and m is the weight of CuO. The calculated specific capacitance values of the Cu/CuO-1, Cu/CuO-2 and Ni/CuO electrodes are shown in Fig. 4(d). The obtained maximum specific capacitance values of 535 $\mathrm{Fg^{-1}}$ for Ni/CuO electrode from the discharge curve at a current density of 2 Ag^{-1} was relatively higher than the binder included electrodes of Cu/CuO-1 and Cu/CuO-2. Also, the capacitance value was found to be higher than the other form of binder-free CuO electrodes recently reported by several others[21-23]. However, in contrast the capacitance value was slightly lower than the CuO sheet arrays on nickel foam as reported by Wang *et al*.[21.]

The excellent capacitance values of the Ni/CuO electrods can be attributed to their structural features. The highly conductive nature of the 3D macroporous Ni foam enables efficient charge transport and accessible diffusion of electrolyte. Further, a good electrical contact between the current collector and the CuO nanoplates efficiently enhances more of the active material to contribute to the capacity i.e., the "dead volume" in the electrode is significantly reduced. Also, the interspaces between the adjacent nanoplates allows easy diffusion of the electrolyte into the nanoplate matrix to provide the large surface area for Faradaic reactions, which allows abundant adsorption of ions as well as enables fast intercalation/de-intercalation of ions and charge transport. In addition, the thin layer of CuO nanoseed layer may also contribute to the enhanced capacitive performance of the electrode.

The specific capacitance values of binder included electrodes of Cu/CuO-1 and Cu/CuO-2 were found to be 230 Fg^{-1} and 296 Fg^{-1} respectively at a current density of 0.7 Ag^{-1}. The desirable high-rate capacitive behavior of Cu/CuO-2 electrode is mainly attributed to the highly mesoporous structure of the electrode with higher surface area (Fig. 2(d)) as compared to Cu/CuO-1, which can significantly facilitate the penetration of protons or other cations into the whole electrode matrix.

To investigate the stability of the Ni/CuO and Cu/CuO-2 electrodes, a cycling test was conducted over 2000 cycles as shown in Figure 5. From the Fig. 5(b), Ni/CuO exhibited lesser degradation even after completion of 2000 repeated sweeps, thus confirming the good cycling stability of the electrode. Interestingly, 94% of the capacity was retained even after 2000 cycle as seen from Fig. 5(b). These results thus, demonstrated the active electrode material i.e. Ni/CuO was very stable during the CV cycling test. Whereas, binder included Cu/CuO-2 electrode exhibited only 89% capacity retention after 2000 cycles (Fig. 5(a)). The capacitance loss is not only caused by the nature of the material by itself but may possibly be due to the continuous oxidation-reduction reactions, which in turn leads to the change in the volume of the active materials. This change thus results in an inefficient binding of the CuO with its PVDF matrix, thereby showing a reduction in their capacity retention.

The electrochemical stability was further confirmed for both electrodes by the charge/discharge measurements as shown in Fig. 5(c) and (d). The results showed an undistorted and essentially symmetric curve even after an extended period of charge and discharge cycles. The capacitance loss was found to be around 16% (~650 cycles) for Cu/CuO-2 electrode at the current density of 1.8 Ag^{-1} while only 11.3% for Ni/CuO electrode (~1000 cycles) even at a higher current density of 4 Ag^{-1}. These results also concluded that the Ni/CuO electrode presents a larger specific capacitance and excellent rate stability, which is a promising feature for the development of high–performance supercapacitors.

Electrochemical impedance spectroscopy (EIS) was studied to understand the interfacial electronic property of the Cu/CuO-1, Cu/CuO-2 and Ni/CuO electrodes in the frequency range of 100 kHz to 10 mHz at an open circuit potential by applying an AC voltage of 10 mV. The Nyquist plots showed capacitive behavior impedance spectra for all the three electrodes (Fig. 6(a)). At higher frequency (Fig 6(a) inset) the impedance spectra showed a distorted semicircle, followed by a linear shape at lower frequency region. The equivalent circuit used for fitting the EIS spectra is as given in the Fig. 6(a) and the electronic components as fitted by the solution resistance (Rs), charge transfer resistance (Rct), Warburg impedance (Zw), constant phase element (CPE) from the double layer and pseudo-faradaic capacitance (C). Ni/CuO exhibits smaller Rs, manifesting the good conductivity of the electrolyte and low internal resistance of the capacitor. The fitted results presented as table in Fig 6(a). The Rct is also fairly low for the Ni/CuO (1.5 **Ω**) when compared to the binder-included electrodes, which indicates the improved ionic conduction and electrolyte diffusion to the CuO nanoplates on Ni foam electrode.

The energy density (ED) and power density (PD) are the two most important parameters of electrochemical supercapacitor devices, which determine the operational performance/efficiency. To investigate the aforesaid properties of CuO nanostructures in a complete cell set up, symmetrical and asymmetrical devices were fabricated for Cu/CuO-2 and Ni/CuO electrodes that showed a better capacitive performance in the three electrode system studies. The symmetrical device composed of CuO nanostructures as the positive and negative electrodes, polypropylene as the separator and stainless steel as the current collectors (Fig. S1). Whereas, activated carbon (AC) was used as negative electrode along with CuO nanostructures as the positive electrode for the fabrication of asymmetrical devices. The CV curves, charge/discharge measurements and the capacitance values from charge/discharge curves of the symmetric devices between 0 and 1.0 V in 6M KOH electrolyte are shown in Fig. S2. The cell maintained the rectangular shape of CVs even at a higher scan rate of 150 mV s^{-1}, indicating ideal capacitive behavior and desirable fast charging/discharging property for power devices. Fig 6(b) and (c) shows the galvanostatic charge/discharge curves of the asymmetric devices at different current densities of both CuO nanostructures, which were used to evaluate the energy and power densities. The CVs and the capacitance values for the devices calculated from the charge/discharge curves are represented in Fig S3. The ED and PD values were calculated by using the following equations[41-42].

$$ED = \frac{1}{2} C_T (\Delta V)^2, PD = (\Delta V)^2 / 4RM \qquad (6)$$

where, $C_{T,}$ ΔV, R, and M are the total capacitance of the entire device, the potential window of discharge, the internal resistance from IR drop, and the total mass of both electrodes, respectively. The internal resistance (IR drop) were determined from the voltage drop at the beginning of the galvanostaic discharge curves.

The Ragone plot for asymmetrical devices is shown in Fig. 6(d). The Ni/CuO electrode delivered a high energy density of about 29.4 Wh/kg at a high power density of 12.7 KW/kg. Further, the Ni/CuO electrode also showed a higher performance compared to the Cu/CuO-2 electrode in symmetric device studies (Fig. S2). All these observations possibly make binder-free Ni/CuO nanoplates electrode to be a promising candidature for supercapacitor applications when compared to the binder-included electrodes of bud and flower shaped CuO nanostructures.

4. Conclusion

Three different morphologies of CuO electrodes, binder-free and binder-included were prepared and investigated for their electrochemical properties. The results showed the binder-free CuO nanoplate electrode on Ni foam to exhibit higher utilization efficiency and better electrolyte diffusion compared to the binder-included electrodes of bud and flower-shaped CuO. An excellent specific capacitance and stable cycling performance characteristic of a supercapacitor was effectively exhibited by the synthesized Ni/CuO electrode. The cost-effective process, availability of the source materials, easy preparation method and better electrochemical properties makes the Ni/CuO nanoplates to be an excellent source for electrode materials in the preparation of supercapacitors.

Acknowledgements

This research was supported by the Basic Science Research Program (Grant No. 2014-010369), Priority Research Centers Program (Grant No. 2009-0093818) and Leader Industry University Cooperation (LINC) project (Grant No. 2014E7268010115) through the National Research Foundation of Korea (NRF) and funded by the Ministry of Education. The author also thanks for Dr. J.-S. Bae of Busan center, KBSI.

References

1. H.-C. Chien, W.-Y. Cheng, Y.-H. Wang and S.-Y. Lu, Adv. Funct. Mater., 2012, 22, 5038-5043.
2. A.S. Arico, P. Bruce, B. Scrosati, J.-M. Tarascon and W. van Schalkwijk, Nat. Mater., 2005, 4, 366-377.
3. X.-M. Liu, Z. d. Huang, S. w. Oh, B. Zhang, P.-C. Ma, M. M. F. Yuen and J.-K. Kim, Compos. Sci. Tech., 2012, 72, 121-144.
4. B. E. Conway, J. Electrochem.l Soc., 1991, 138, 1539-1548.
5. R. Kötz and M. Carlen, Electrochim. Acta, 2000, 45, 2483-2498.
6. E. Frackowiak and F. Béguin, Carbon, 2002, 40, 1775-1787.
7. W. Yong-gang and Z. Xiao-gang, Electrochim. Acta, 2004, 49, 1957-1962.
8. K. Xie, X. Qin, X. Wang, Y. Wang, H. Tao, Q. Wu, L. Yang and Z. Hu, Adv. Mater., 2012, 24, 347-352.

9. X. He, R. Li, J. Qiu, K. Xie, P. Ling, M. Yu, X. Zhang and M. Zheng, Carbon, 2012, 50, 4911-4921.
10. L. Zhang and G. Shi, J. Phys. Chem. C, 2011, 115, 17206-17212.
11. X. Zhao, B. M. Sanchez, P. J. Dobson and P. S. Grant, Nanoscale, 2011, 3, 839-855.
12. G. Wang, L. Zhang and J. Zhang, Chem. Soc. Rev., 2012, 41, 797-828.
13. C. Yuan, J. Li, L. Hou, X. Zhang, L. Shen and X. W. Lou, Adv. Funct. Mater., 2012, 22, 4592-4597.
14. J. Jiang, J. Liu, R. Ding, J. Zhu, Y. Li, A. Hu, X. Li and X. Huang, ACS Appl. Mater. Interfaces, 2010, 3, 99-103.
15. H. Jiang, T. Zhao, C. Yan, J. Ma and C. Li, Nanoscale, 2010, 2, 2195-2198.
16. H. Jiang, T. Zhao, J. Ma, C. Yan and C. Li, Chem. Commun., 2011, 47, 1264-1266.
17. K. R. Prasad and N. Miura, Appl. Phys. Lett., 2004, 85, 4199-4201.
18. V. Srinivasan and J. W. Weidner, J. Power Sources, 2002, 108, 15-20.
19. R. N. Reddy and R. G. Reddy, J. Power Sources, 2003, 124, 330-337.
20. H. Zhang, J. Feng and M. Zhang, Mater. Res. Bull., 2008, 43, 3221-3226.
21. G. Wang, J. Huang, S. Chen, Y. Gao and D. Cao, J. Power Sources, 2011, 196, 5756-5760.
22. Y.-K. Hsu, Y.-C. Chen and Y.-G. Lin, J. Electroanal. Chem., 2012, 673, 43-47.
23. L. Yu, Y. Jin, L. Li, J. Ma, G. Wang, B. Geng and X. Zhang, Cryst. Eng. Comm., 2013, 15, 7657-7662.
24. B. Vidhyadharan, I. I. Misnon, R. A. Aziz, K. P. Padmasree, M. M. Yusoffa and R. Jose, J. Mater. Chem. A, 2014, 2, 6578–6588
25. J. Pike, S.-W. Chan, F. Zhang, X. Wang and J. Hanson, Appl. Catal. A, 2006, 303, 273-277.

26. Y. Duan, J. F. Kong and W. Z. Shen, J. Raman Spectros., 2012, 43, 756-760.
27. J. C. Irwin, J. Chrzanowski, T. Wei, D. J. Lockwood and A. Wold, Physica C, 1990, 166, 456-464.
28. J. F. Xu, W. Ji, Z. X. Shen, S. H. Tang, X. R. Ye, D. Z. Jia and X. Q. Xin, J. Solid State Chem., 1999, 147, 516-519.
29. Z. Ye, L. Hu, J. Jiang, J. Tang, X. Cao and H. Gu, Catal. Sci. Tech., 2012, 2, 1146-1149.
30. Y. C. Zhang, J. Y. Tang, G. L. Wang, M. Zhang and X. Y. Hu, J. Cryst. Growth, 2006, 294, 278-282.
31. Z. Zhang and P. Wang, J. Mater.Chem., 2012, 22, 2456-2464.
32. S. Poulston, P. M. Parlett, P. Stone and M. Bowker, Surf. Interface Anal., 1996, 24, 811-820.
33. J. F. Moulder, W. F. Stickle, P. E. Sobol and K. D. Bomben, Handbook of X-ray photoelectron spectroscopy, Perkin Elmer Eden Prairie, MN, 1992.
34. M. Yin, C.-K. Wu, Y. Lou, C. Burda, J. T. Koberstein, Y. Zhu and S. O'Brien, J. Am. Chem. Soc., 2005, 127, 9506-9511.
35. M. F. Al-Kuhaili, Vacuum, 2008, 82, 623-629.
36. S. K. Meher and G. R. Rao, Nanoscale, 2013, 5, 2089-2099.
37. Y.-C. Chen, Y.-K. Hsu, Y.-G. Lin, Y.-K. Lin, Y.-Y. Horng, L.-C. Chen and K.-H. Chen, Electrochim. Acta, 2011, 56, 7124-7130.
38. N. Mukherjee, B. Show, S. K. Maji, U. Madhu, S. K. Bhar, B. C. Mitra, G. G. Khan and A. Mondal, Mater. Lett., 2011, 65, 3248-3250.
39. M-J. Deng, C-C. Wang, P-J. Ho, C-M. Lin, J-M. Chen and K-T. Lu, J. Mater. Chem. A, 2014, 2, 12857-12865

40. Y. X. Zhang, M. Huang, F. Li, Z. Q. Wen, Int. J. Electrochem. Sci., 2013, 8, 8645 – 8661.
41. B.G. Choi, M.H. Yang, W. H. Hong, J. W. Choi, and Y. S. Huh, ACS Nano, 2012, 6(5), 4020–4028.
42. J. Ji , L. L. Zhang, H. Ji , Y. Li, X. Zhao, X. Bai, X. Fan, F. Zhang , and R.S. Ruoff, ACS Nano, 2013, 7(7), 6237–6243.

Figure captions

Fig. 1. FE-SEM images of the CuO with low and high magnifications and corresponding EDX images. (a-d) 6 hrs (bud shaped-CuO), (e-h) 18 hrs (flower shaped-CuO) and (i-l) CuO nanoplates on Ni foam.

Fig. 2. (a) XRD pattern of copper oxide nanostructures with standard JCPDS card data. (b) Raman spectra of the CuO nanostructures of Cu/CuO-1, Cu/CuO-2 and Ni/CuO. (c) XPS-Cu 2*p* core level and O 1*s* binding energy spectrum of the Cu/CuO-2 sample. (d) Isothermal N_2 adsorption-desorption curves of Cu/CuO-1 and Cu/CuO-2 samples, the insets in the isothermal plots represent the pore size distribution curves.

Fig. 3. Cyclic voltammograms of the prepared copper oxide electrodes in 6M KOH aqueous solution (a) Ni foam and Cu bare substrates (b) Cu/CuO-1 (c) Cu/CuO-2 and (d) Ni/CuO. (Inset-(b-d) square root of voltage scan rate ($v^{1/2}$) vs cathodic peak current (i_p))

Fig. 4. Galvanostatic charge/discharge results and the specific capacitance values of CuO nanostructures. (a) Cu/CuO-1 (b) Cu/CuO-2 (c) Ni/CuO, and (d) specific capacitance values of three CuO electrodes.

Fig.5. Variation of capacity retention with number of cycles. (a) Cu/CuO-2 and (b) Ni/CuO. (Inset-(a) & (b) CV curves). Results of charge/discharge cycles over 10^5 seconds (c) Cu/CuO-2 and (d) Ni/CuO

Fig. 6. (a) Electrochemical impedance spectrum of the CuO electrodes. The charge/discharge measurements with different current densities of CuO nanostructures by asymmetrical devices. (b) Cu/CuO-2 (c) Ni/CuO (the inset figure demonstrates a light-emitting-diode (LED) powered by asymmetrical Ni/CuO//AC device) and (d) Ragone plots of power density vs. energy density of the CuO electrodes.

Figures

Figure. 1

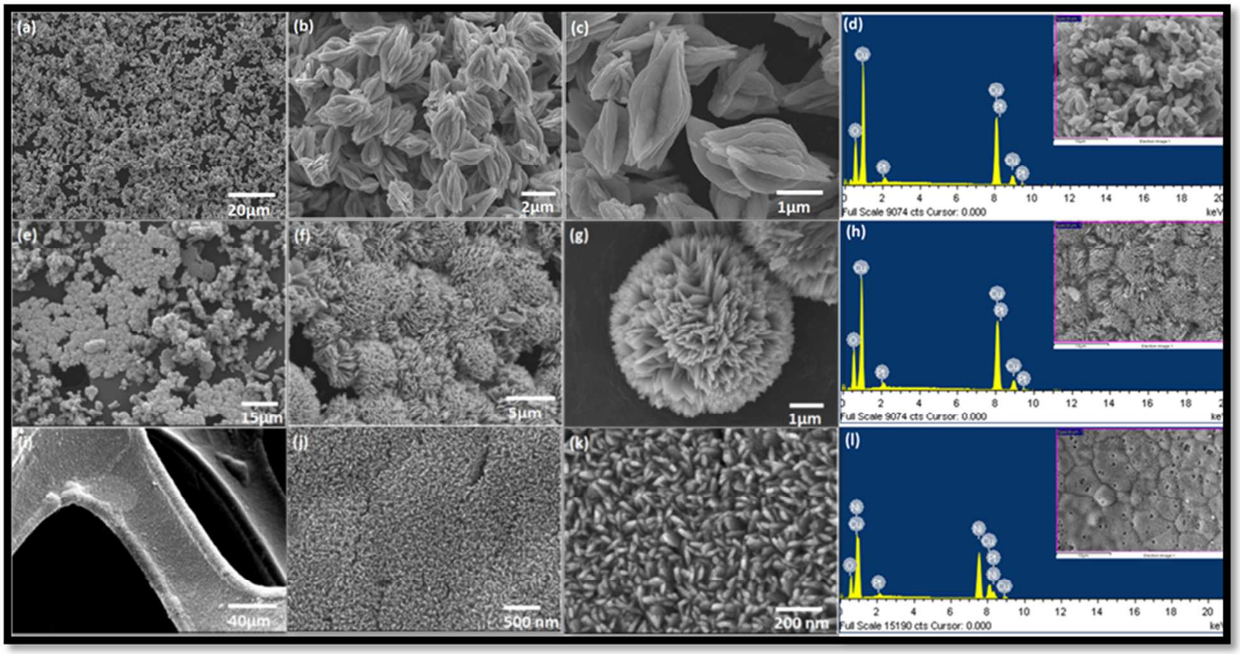

Figure. 2

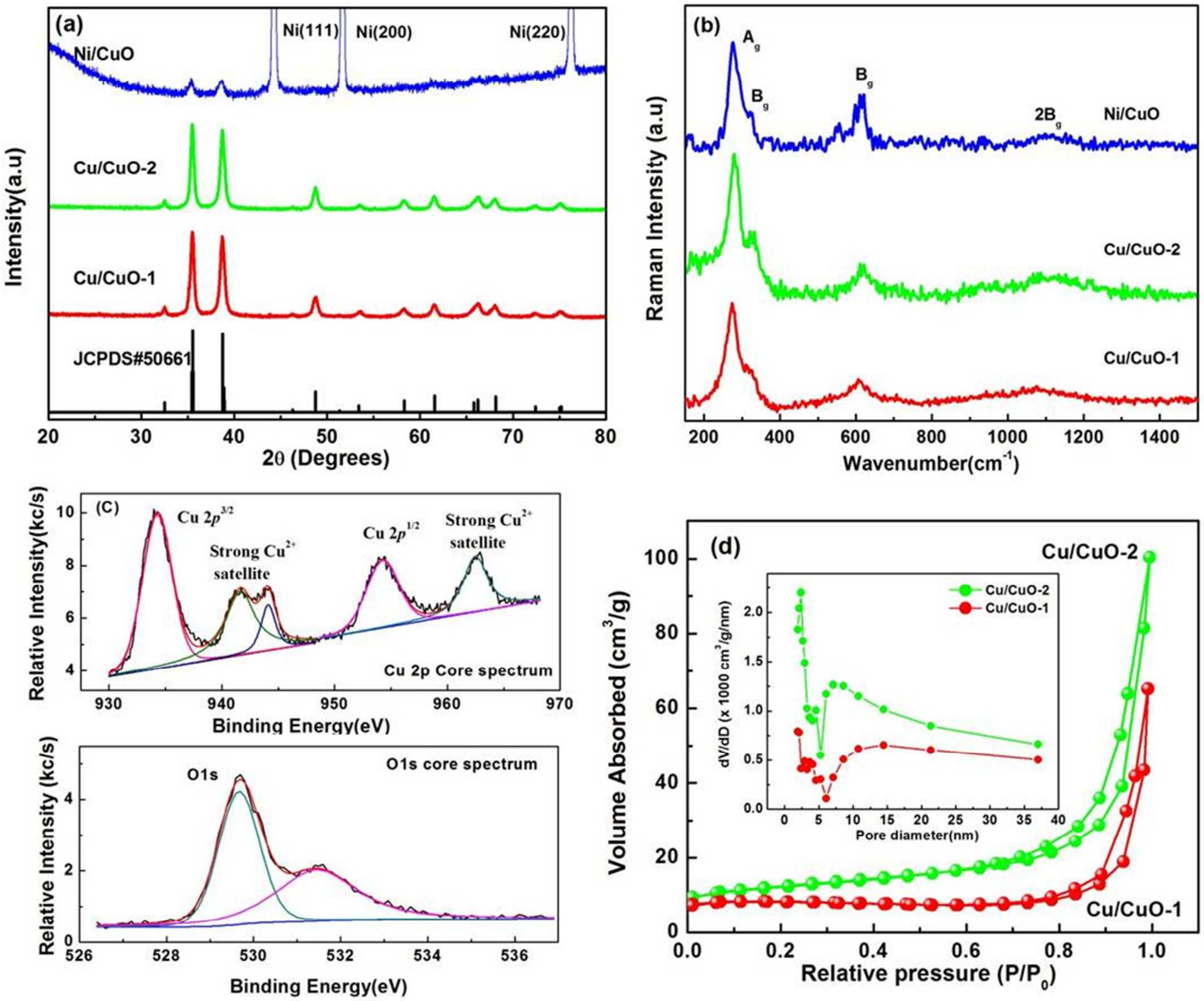
(a)
Ni/CuO
Ni(111)
Ni(200)
Ni(220)
Cu/CuO-2
Cu/CuO-1
JCPDS#50661
Intensity(a.u)
2θ (Degrees)
20
30
40
50
60
70
80
(b)
A_g
B_g
B_g
2B_g
Ni/CuO
Cu/CuO-2
Cu/CuO-1
Raman Intensity (a.u)
Wavenumber(cm⁻¹)
200
400
600
800
1000
1200
1400
(C)
Cu 2p3/2
Strong Cu2+ satellite
Cu 2p1/2
Strong Cu2+ satellite
Cu 2p Core spectrum
Relative Intensity(kc/s)
Binding Energy(eV)
930
940
950
960
970
O1s
O1s core spectrum
Relative Intensity (kc/s)
Binding Energy(eV)
526
528
530
532
534
536
(d)
Cu/CuO-2
Cu/CuO-1
Volume Absorbed (cm³/g)
Relative pressure (P/P0)
dV/dD (x 1000 cm³/g/nm)
Pore diameter(nm)
Cu/CuO-2
Cu/CuO-1

Figure.3

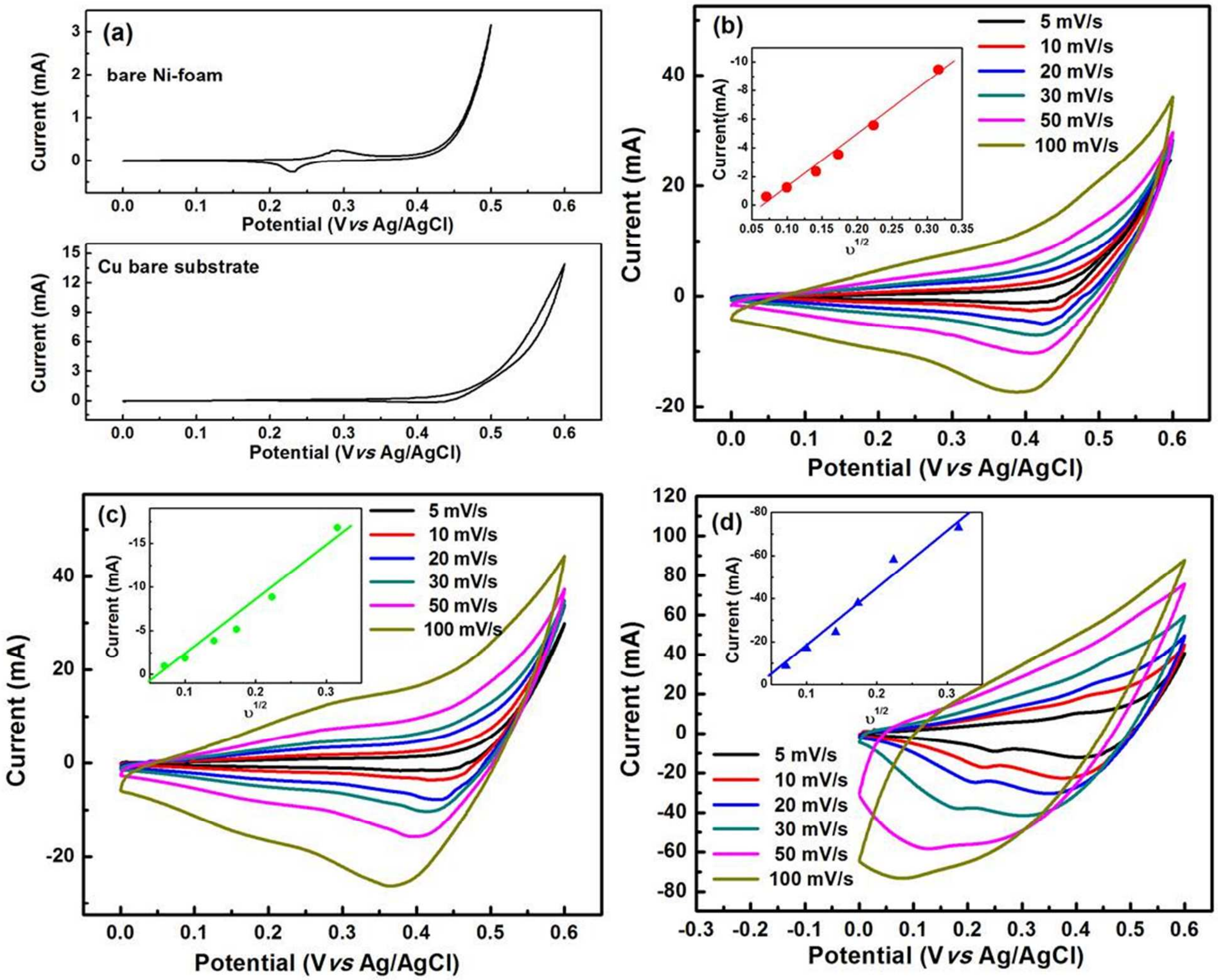
(a)
bare Ni-foam
Current (mA)
3
2
1
0
0.0 0.1 0.2 0.3 0.4 0.5 0.6
Potential (V *vs* Ag/AgCl)
Cu bare substrate
Current (mA)
15
12
9
6
3
0
0.0 0.1 0.2 0.3 0.4 0.5 0.6
Potential (V *vs* Ag/AgCl)
(b)
5 mV/s
10 mV/s
20 mV/s
30 mV/s
50 mV/s
100 mV/s
Current (mA)
40
20
0
-20
0.0 0.1 0.2 0.3 0.4 0.5 0.6
Potential (V *vs* Ag/AgCl)
Current(mA)
-10
-8
-6
-4
-2
0
0.05 0.10 0.15 0.20 0.25 0.30 0.35
$\upsilon^{1/2}$
(c)
5 mV/s
10 mV/s
20 mV/s
30 mV/s
50 mV/s
100 mV/s
Current (mA)
40
20
0
-20
0.0 0.1 0.2 0.3 0.4 0.5 0.6
Potential (V *vs* Ag/AgCl)
Current (mA)
-15
-10
-5
0
0.1 0.2 0.3
$\upsilon^{1/2}$
(d)
120
100
80
60
40
20
0
-20
-40
-60
-80
Current (mA)
-0.3 -0.2 -0.1 0.0 0.1 0.2 0.3 0.4 0.5 0.6
Potential (V *vs* Ag/AgCl)
5 mV/s
10 mV/s
20 mV/s
30 mV/s
50 mV/s
100 mV/s
Current (mA)
-80
-60
-40
-20
0
0.1 0.2 0.3
$\upsilon^{1/2}$

Figure. 4

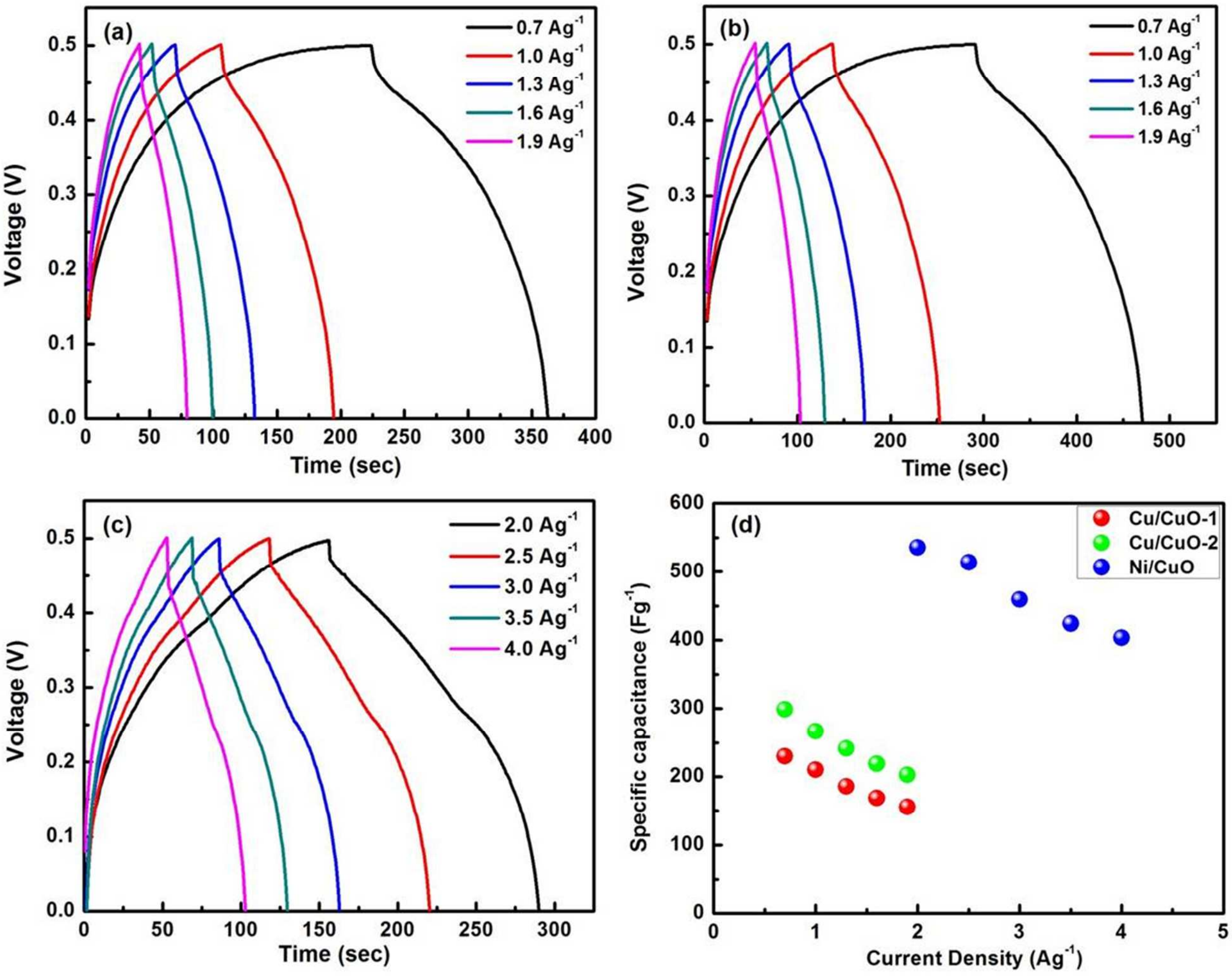
(a)
0.7 Ag^{-1}
1.0 Ag^{-1}
1.3 Ag^{-1}
1.6 Ag^{-1}
1.9 Ag^{-1}
Voltage (V)
0.0
0.1
0.2
0.3
0.4
0.5
Time (sec)
0
50
100
150
200
250
300
350
400
(b)
0.7 Ag^{-1}
1.0 Ag^{-1}
1.3 Ag^{-1}
1.6 Ag^{-1}
1.9 Ag^{-1}
Voltage (V)
Time (sec)
0
100
200
300
400
500
(c)
2.0 Ag^{-1}
2.5 Ag^{-1}
3.0 Ag^{-1}
3.5 Ag^{-1}
4.0 Ag^{-1}
Voltage (V)
Time (sec)
0
50
100
150
200
250
300
(d)
Cu/CuO-1
Cu/CuO-2
Ni/CuO
Specific capacitance (Fg^{-1})
0
100
200
300
400
500
600
Current Density (Ag^{-1})
0
1
2
3
4
5

Figure. 5

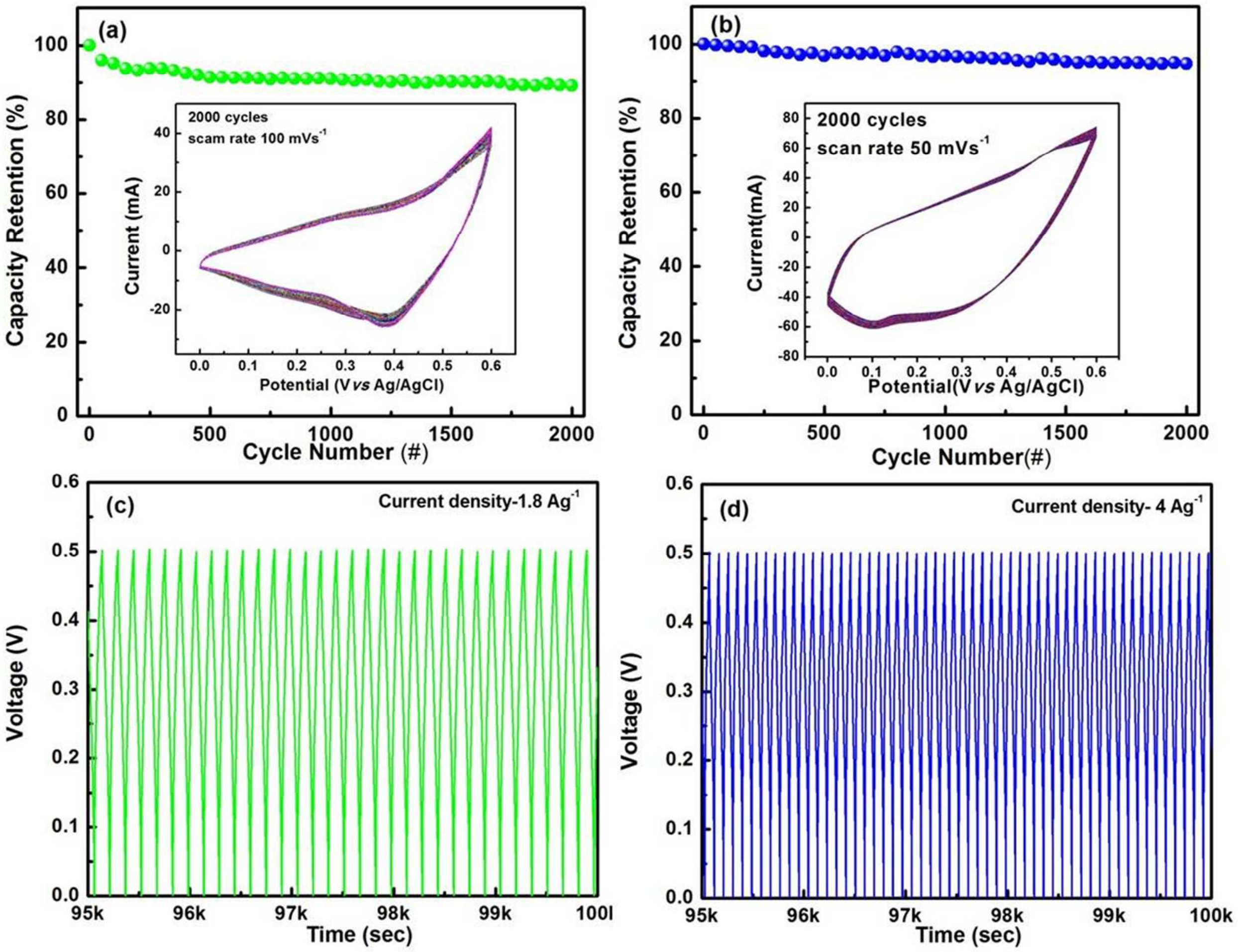
(a)
Capacity Retention (%)
100
80
60
40
20
0
0
500
1000
1500
2000
Cycle Number (#)
2000 cycles
scam rate 100 mVs^{-1}
Current (mA)
40
20
0
-20
0.0
0.1
0.2
0.3
0.4
0.5
0.6
Potential (V vs Ag/AgCl)
(b)
Capacity Retention (%)
100
80
60
40
20
0
0
500
1000
1500
2000
Cycle Number(#)
2000 cycles
scan rate 50 mVs^{-1}
Current(mA)
80
60
40
20
0
-20
-40
-60
-80
0.0
0.1
0.2
0.3
0.4
0.5
0.6
Potential(V vs Ag/AgCl)
(c)
Current density-1.8 Ag^{-1}
Voltage (V)
0.6
0.5
0.4
0.3
0.2
0.1
0.0
95k
96k
97k
98k
99k
100l
Time (sec)
(d)
Current density- 4 Ag^{-1}
Voltage (V)
0.6
0.5
0.4
0.3
0.2
0.1
0.0
95k
96k
97k
98k
99k
100k
Time (sec)

Figure. 6

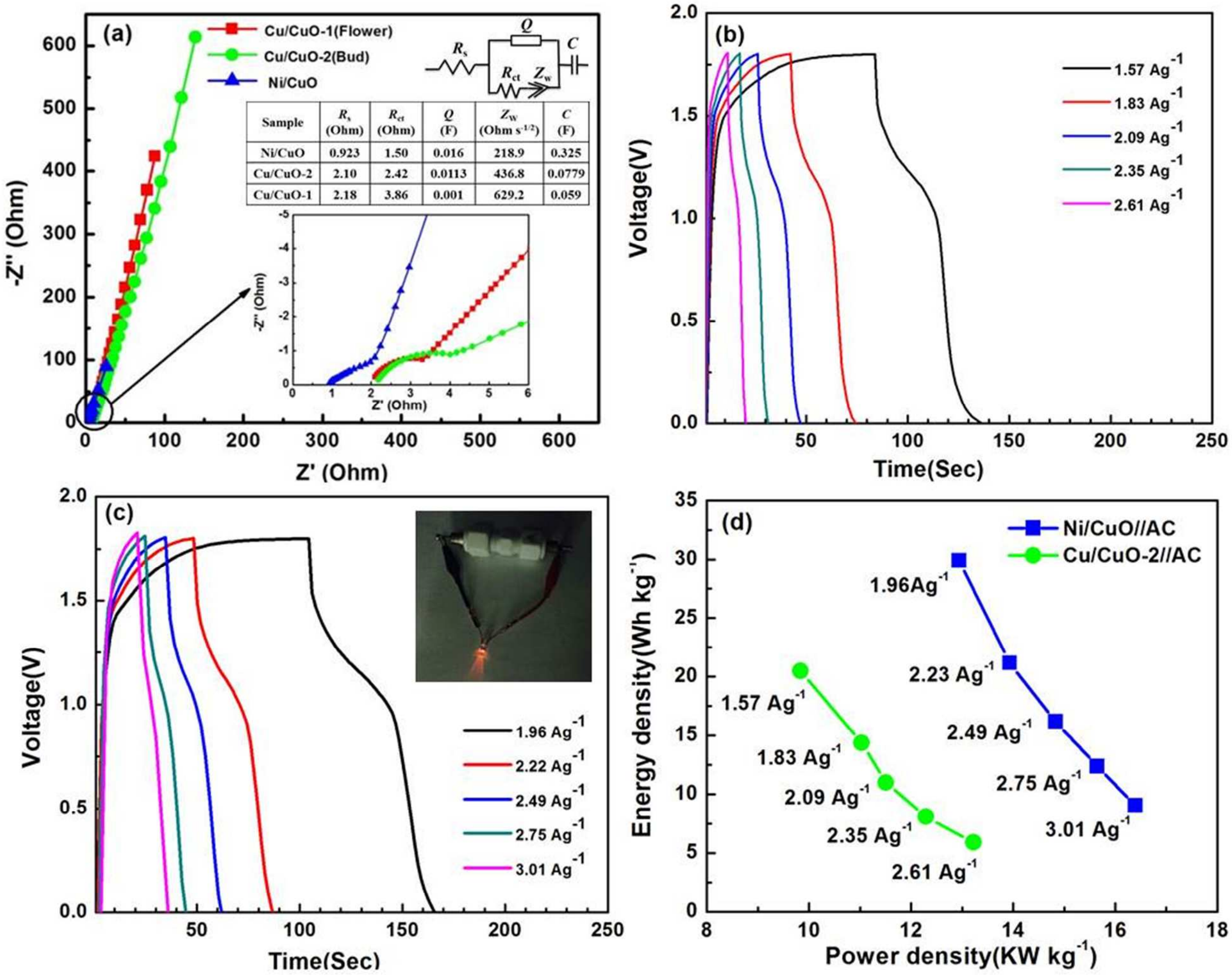

Sample	R_s (Ohm)	R_{ct} (Ohm)	Q (F)	Z_W (Ohm s$^{-1/2}$)	C (F)
Ni/CuO	0.923	1.50	0.016	218.9	0.325
Cu/CuO-2	2.10	2.42	0.0113	436.8	0.0779
Cu/CuO-1	2.18	3.86	0.001	629.2	0.059